Near-Field Effects in Radio Frequency Emission from Particle Showers in a Dense Medium
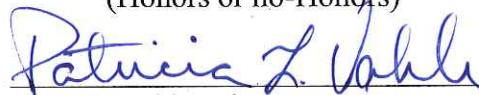
A thesis submitted in partial fulfillment of the requirement
for the degree of Bachelor of Arts / Science in Physics from
The College of William and Mary
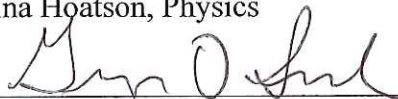
by

Rachel Jordan Hyneman

Accepted for HONORS
_____
(Honors or no-Honors)

Patricia L. Vahle

Patricia Vahle, Director

Gina L. Hoatson

Gina Hoatson, Physics

Gregory Smith

Gregory Smith, Applied Sciences

Williamsburg, VA
April 30, 2015

Near-Field Effects in Radio Frequency Emission from Particle Showers in a Dense Medium

Rachel Hyneman, *College of William & Mary*

Advisors: Dr. Patricia Vahle, *College of William & Mary*

Dr. Stephanie Wissel, *University of California, Los Angeles*

May 4, 2015

Abstract

The SLAC T-510 Experiment studied the effects of a magnetic field upon the radio-frequency emission from particle showers in high-density polyethylene. Ultra-High Energy (UHF) and Very High Frequency (VHF) antennas were used to measure the radio frequency (RF) radiation from particle showers in the target. Special near field data runs were performed with the UHF antenna array positioned closer to the target (along the beam axis). The signal was split into two linearly polarized components, vertical and horizontal, arising from two different mechanisms: the Askaryan and Magnetic effects, respectively. Peak voltage data from the near-field runs was used to determine the behavior of the radiation amplitude as a function of distance from the target and angle made with respect to the beam line. Power spectral densities were produced using near field runs to analyze how various frequency ranges behaved as a function of

distance. Initial results indicate that the amplitude dependence of the peak voltage on angle remains consistent even as the antennas are moved further from the target. A $\frac{1}{R}$ correction describes the effects of moving away from the target well. Spectral analysis reveals unclear effects in the lower frequency ranges. Although near field interference might be expected, such variations are likely dominated by reflections of RF emission within the target.

1   Introduction

1.1   The ANITA Experiment

The Antarctic Transient Antenna (ANITA) Experiment is a balloon-borne experiment focused on the detection of ultra-high energy cosmic rays (UHECRs) and ultra-high energy neutrinos. The apparatus consists of an array of sensitive radio-frequency (RF) antennas which are carried by balloon above Antarctica. The antennas are capable of detecting radio frequency (RF) emission from particle showers induced by ultra-high energy particles colliding with secondary particles in the earth's atmosphere and within the Antarctic ice. To date, ANITA has identified 16 events believed to be UHECRs [4]. Most recently, ANITA III ran in December of 2014 through January 2015, and data analysis, as well as preparations for a fourth ANITA run, are currently underway.

The experiment relies on three interesting phenomena, the Askaryan effect, the Geo-magnetic effect, and Cherenkov amplification, in order to detect particle shower RF emission. When an ultra-high energy particle enters the earth's atmosphere, it collides with other atmospheric particles. The high energy collisions produce a cascade of secondary particles, which in turn may collide or decay. While the dynamics of the

full-scale shower are complicated, the shower primarily consists of electron, positrons, muons and photons once it has fully developed [7]. Because of the electrons in the atmosphere, though, many of the shower's positrons will annihilate, leaving a significant charge imbalance in the particle shower. In addition to the annihilation imbalance, extra electrons may be excited via Compton scattering from γ rays emitted from shower collisions. The total charge imbalance, called the Askaryan effect, means that the particle shower carries a net negative charge which propagates on average in a set direction, the shower axis. Hence, the shower, a coherent, moving charge distribution, will radiate, and this radiation falls within the RF range [1]. A previously conducted experiment at the SLAC National Accelerator Laboratory confirmed theoretical expectations of Askaryan radiation in ice [3] and paved the way for the ANITA experiment. As expected from moving charge, the Askaryan radiation is directed radially outward from the shower axis, as shown in Figure 1
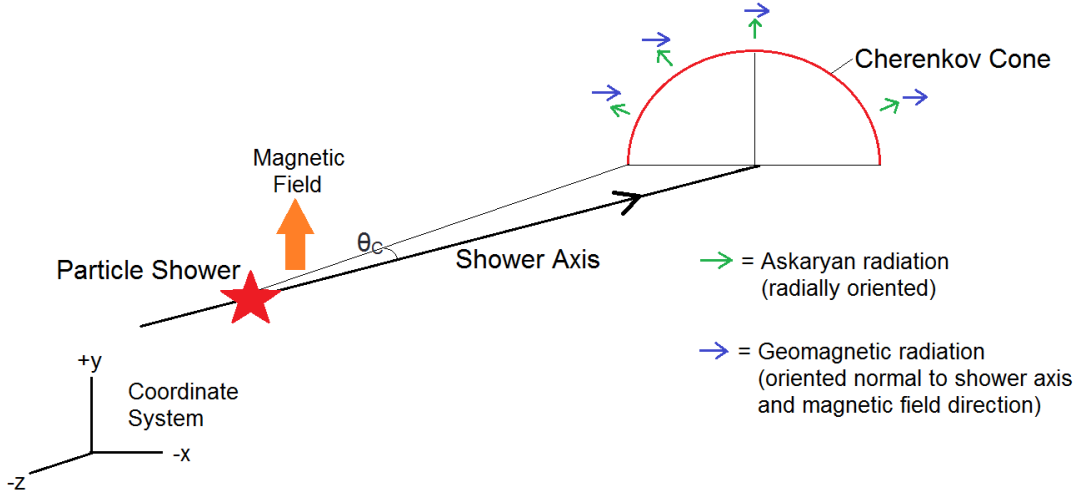

Figure 1: Diagram of Emission Mechanisms

The second important phenomena, the Geo-magnetic effect, results from interaction

3

between the particle shower and the earth's magnetic field. As the charged particles in the shower propagate through the magnetic field, the positrons and electrons separate, forming a current transverse to the direction of propagation. An electric field is induced between the positive and negative components of the shower, resulting in radiation polarized in a direction perpendicular to the shower axis and to the direction of Earth's magnetic field, as shown in Figure 1. The Geo-magnetic radiation's telltale polarization is key to identifying observed RF pulses as UHECR events [4].

The third phenomena, Cherenkov amplification, is the effective amplification of electromagnetic radiation at a specific angle, θ_C, where

$$\cos \theta_c = \frac{1}{n\beta}$$

such that n is the index of refraction of the material and $\beta = v_{phase}/c$ (in many materials, $\beta \approx 1$). In a medium, high energy shower particles will travel at relativistic speeds that can exceed the speed of light in that medium. The results are analogous to a sonic boom seen from a moving noise source. An observer standing at an angle θ_C with respect to the shower axis will effectively observe the radiation from the entire development of the shower instantaneously, and because the shower is azimuthally symmetric, the Cherenkov angle can be extended to form a uniform Cherenkov cone (as shown in Figure 1). In addition, an observer located along the Cherenkov cone with vertex located at x_{max} (the location along the shower axis with the largest number of propagating shower particles) will observe a significantly larger signal from the shower, even if otherwise the emission would have been very small.

4

1.2 the SLAC T-510 Experiment

The SLAC T-510 Experiment was performed primarily by members of the ANITA collaboration, as well as members of other UHECR and ultra-high energy neutrino experiments. The goal of the experiment is to examine the magnetic radiation in a controlled environment for purposes of calibration of ANITA data analysis [2]. A particle shower was induced in a target of high-density polyethylene using SLAC's electron beam. UHF antennas from a previous ANITA run, VHF antennas and a Long Periodic Dipole Array (LPDA) were used to measure the RF emission from the particle shower induced in the polyethylene. By comparing the data to simulation, the ANITA experiment may calibrate its Monte Carlo simulations of atmospheric particle showers and their RF emission, which are critical to reconstructing primary particle energy. On a larger scale, the experiment will better the astro-particle community's understanding of the complex electrodynamics of a particle shower in the presence of a magnetic field.

Another goal of the T-510 Experiment is to understand the effects of being in the "near-field" zone of the RF emission from a particle shower. Within a distance on the order of magnitude of a wavelength away from a radiation source, interference effects may dominate emission, convoluting the expected $\frac{1}{R}$ dependence of the amplitude [5]. The approximate border between the near- and far-field regions falls at:

$$R = \frac{2L^2}{\lambda}$$

where L is the length of the antenna and λ is the wavelength of the radiation [6]. For an antenna with an L value of 1 meter and low-frequency sensitivity to 200 MHz (a good estimate for the UHF antennas used), the near-field zone falls within about 1.3 meters. Radio-frequency electromagnetic waves from particle showers may have wavelengths on

the order of anywhere between $10^{-1} - 10^4$ meters, and so we would expect to observe some of these near-field effects within both T-510 and ANITA data. Understanding near-field effects may lead to more accurate correction techniques in both ANITA III data and in other RF-UHECR experiments.
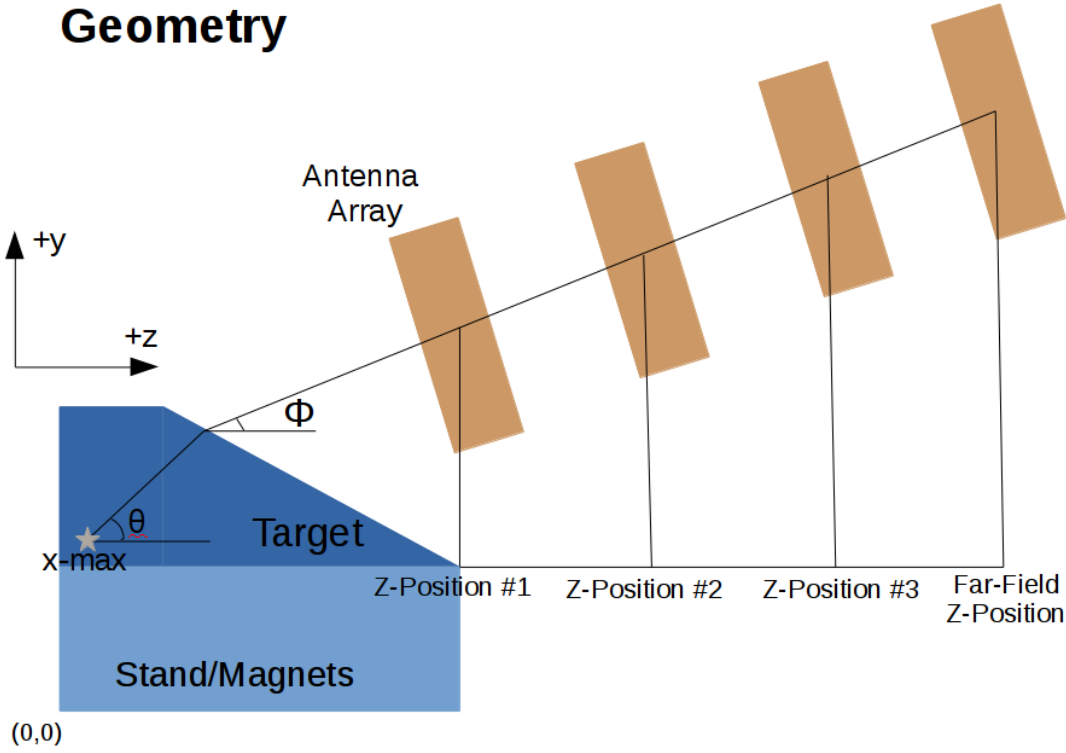
2   Experimental Setup and Geometry

Figure 2: Geometry Diagram

The SLAC T-510 experiment took place in January and February of 2014 in End Station A of the SLAC National Accelerator Laboratory. SLAC's End Station Test Beam (ETSB) was used as a source of electrons with a known energy of approximately 4.35 GeV. An S-Band antenna (an antenna sensitive to 2-4 GHz) was placed near the beam line, upstream of the target, in order to measure beam current for calibration

purposes. A block of high-density polyethylene (HDPE) resembling a triangular prism was placed in the beam path. HDPE was chosen since its density allowed for a more compact shower than would take place in air, and preliminary simulations indicated that the material would produce strong emission. The top of the target is angled as to avoid total internal reflection of the radiation near x_{max}. A 1.2 cm lead pate was placed directly against the edge of the target where the beam entered in order to shorten the length of the particle shower in the target.

The expected index of refraction for high-density polyethylene is 1.53. Therefore, the expected Cherenkov angle is approximately $\theta_C = 49°$ with respect to the beam axis. Due to refraction at the target-air border, the Cherenkov angle outside of the target is approximately 41.5°. For a more direct comparison, the angle θ inside the target must be extracted numerically from the geometry. Underneath the target were placed magnetic coils with a controllable current and current direction. The coils were arranged such as to provide an approximately uniform field of up to $\sim$ 1000 Gauss in the $\pm y$ direction.

An array of four 200-1200 MHz UHF quad-ridged antennas were connected in a vertical line to a frame. (Data taken using the 30-1000 MHz VHF bicone antenna and the microwave-sensitive LPDA will not be addressed in this paper). The frame was angled at 19.6° with respect to vertical, and the frame was adjusted via ropes and the End Station A crane to various positions in relation to the target. For all runs of interest to this analysis, the array was positioned along the beam axis (z axis) and at various heights (y positions). The (z,y) coordinates of the array were measured from the center-height of the front of the array, with $z = 0$ set at the front edge of the target and $y = 0$ set at the ground level. The majority of runs were taken at a z position

of 13.47 meters (the far-field position) and at a wide range of heights. Near-field runs were taken with (z,y) positions of (3.97 m, 4.65 m), (7.00 m, 5.96 m) and (9.90 m, 7.55 m). A reference far field position of (13.47 m, 8.80 m) was chosen for comparison due to it falling at approximately the same $z - y$ angle of the near-field runs. At each of these positions, data was taken with no magnetic field, a positive magnetic field (of $\sim$ 1000 Gauss) and an approximately equivalent negative magnetic field. The run positions were chosen to be directly above the beam axis. As can be seen in Figure 1, the Askaryan component of the emission above the beam line is purely vertical due to its radial orientation. The magnetic component is purely horizontal above the beam line. Therefore, along a a vertical slice above the beam, the two radiation mechanisms can be separated purely by polarization. The experimental geometry is depicted in Figure 2.

Each antenna in the array was connected via an LMR240 coax cable and BLP-1250 low-pass filter to an oscilloscope, which remotely recorded the voltage measured by each antenna in both the horizontal and vertical polarizations over time. Rather than a continuous beam, the SLAC electron beam is rather a series of tightly spaced electron packets. Each packet causes an individual shower within the HDPE target, and the resulting pulse was measured by each scope. An S-band horn antenna, placed near the beam line upstream of the target to measure transition radiation, and an integrating charge transformer were used to monitor fluctuations in beam current. A 12dB attenuator was used in the near field runs, since voltages were expected to be significantly larger in magnitude than in the far field case.

3 Data and Analysis

3.1 Analysis Code

An analysis code in Python was written primarily by Stephanie Wissel following the T-510 experiment for the purposes of data analysis from the experiment. The code primarily corrects the raw data for cable loss (signal loss due to resistance in the cable length), fluctuations in beam current, antenna response variations, cross-polarization interference and the difference between the antenna bore-sight angle (normal to the antenna face) and the angle formed by the incoming radiation.

Cross-polarization leakage (the contamination of signal in one polarization by that of another due to antenna and alignment imperfections) was corrected for in the horizontal polarization by comparing the signals of events with the same conditions except for opposite magnetic field direction. Since the horizontal component should flip with the sign change of the magnetic field, positive- and negative-magnetic field voltage pulses can be added together to eliminate the signal. The remainder can be inferred to be a result of uncorrelated noise and leakage from the vertically polarized feed on the quad-ridged horns. The peak voltage of each event was also scaled according to the reading in the S-band antenna and normalized to an average S-band current of 134 pC. A $200 - -1200$ MHz band pass filter was applied to the waveforms, as well.

The code outputs information from the run data, including the height of each individual antenna, the voltage waveform recorded for each antenna in both horizontal and vertical polarizations, the Fourier transform of the waveform and the z- and y-positions of each individual antenna.

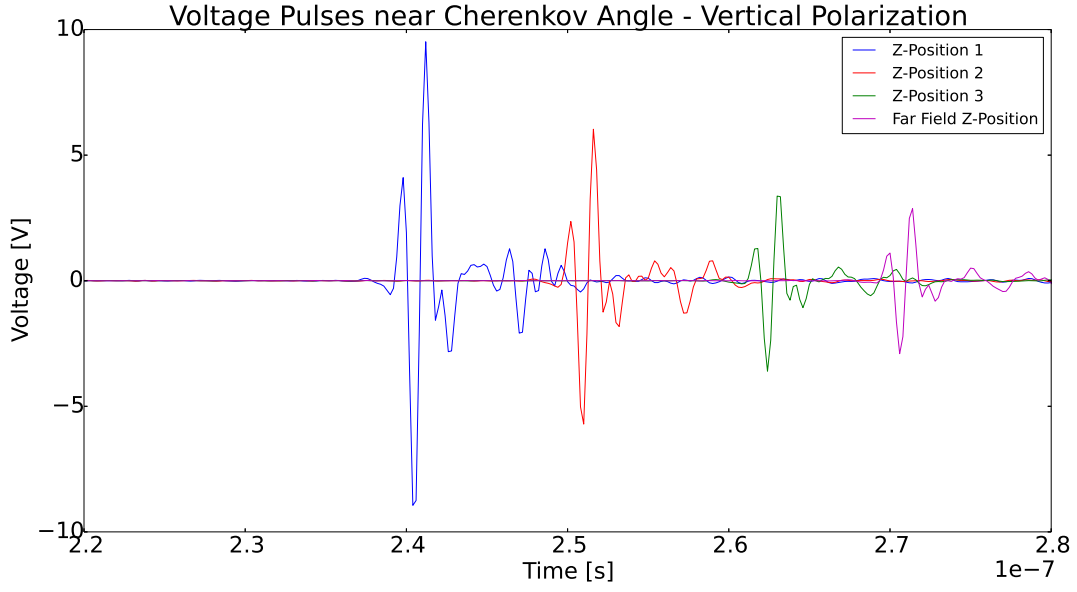Examples of voltage waveforms (averaged over approximately 50 runs) can be

Figure 3: Averaged Voltage Pulse Seen by Antenna Closest to θ_C (V-Pol Component)
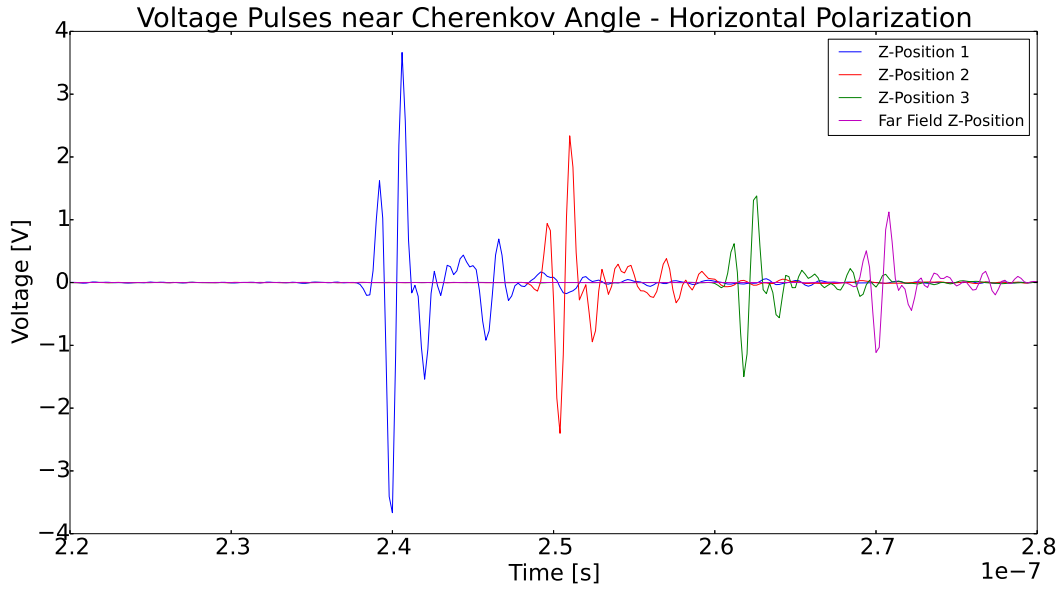

Figure 4: Averaged Voltage Pulse Seen by Antenna Closest to θ_C (H-Pol Component)

viewed in Figures 3 and 4. These voltage pulses show the horzintal component of the emission and are taken from the antenna closest to the Cherenkov angle at each z-position. Notably, the pulses appear to contain reflections which may result from

10

the emission from the shower reflecting off the bottom of the target and reaching the antenna later than the initial radiation.

A separate Python function was written to numerically determine the angle θ formed inside the target along the path taken by radiation traveling from x_{max} to the center of the antenna face. The code traces the path inside the target taken by radiation emitted from the point of beam entry with a half-degree precision. The distance between the antenna position and point of exit of the radiation is calculated along with the defracted angle taken by the radiation outside the target. The path taken at the given angle for the given distance is used to determine the endpoint position of the radiation. The code then minimizes the difference between this endpoint distance and the true antenna position.

By determining the angle θ, a direct comparison can be made to determine the angular deviation from the Cherenkov angle θ_c. The angle θ can be visualized as shown in the geometry image, Figure 2. Note that due to refraction effects, the angle θ is not the arctangent of y/z.

3.2   Far Field Data

The first step taken in data analysis was to generate a plot depicting the horizontal and vertical components of the peak voltage as a function of the angle θ inside the target, for the far field data, also called a "cone plot." Peak voltage data was plotted from both positive and negative magnetic field runs as a function of θ (made inside the target with respect to the beamline), and the resulting plot is shown in Figure 5. Each event (corresponding to a beam spill) for each antenna in each run is shown. Plot markers were chosen such that a triangle pointing up represents the voltage measured in a

positive magnetic field run, while a downward pointing triangle represents a negative magnetic field run. Since Askaryan radiation is polarized radially outward from the beam axis, it would be expected that the vertically polarized (V-Pol) radiation along the vertical stripe of the Cherenkov cone would be a result of the Askaryan effect. Magnetic radiation, however, is polarized perpendicular to the beam axis and the magnetic field direction, and so would be expected to account for the horizontally polarized (H-pol) component.
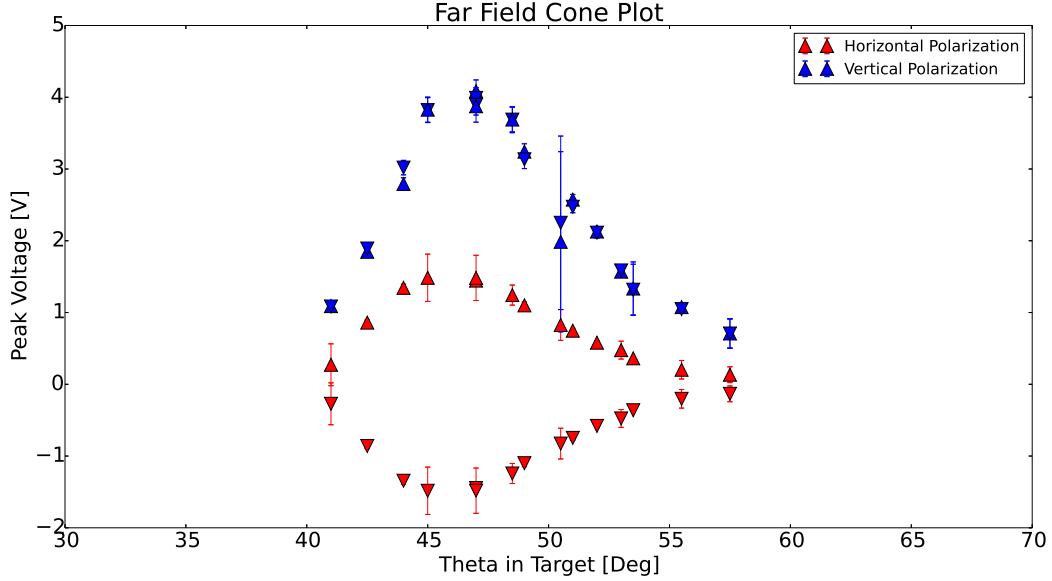
Figure 5: Far Field Cone Plot

The peak V-Pol voltage shows no dependence on the magnetic field, as indicated by the presence of only a single curve for both positive and negative magnetic field runs. This independence supports the assumption that the mechanism behind the V-Pol component of the radiation is purely Askaryan and not magnetic. The peak H-Pol voltage, on the other had, shows a clear dependence on the magnetic field, as evidenced by the presence of two mirror-image curves corresponding to the two magnetic field
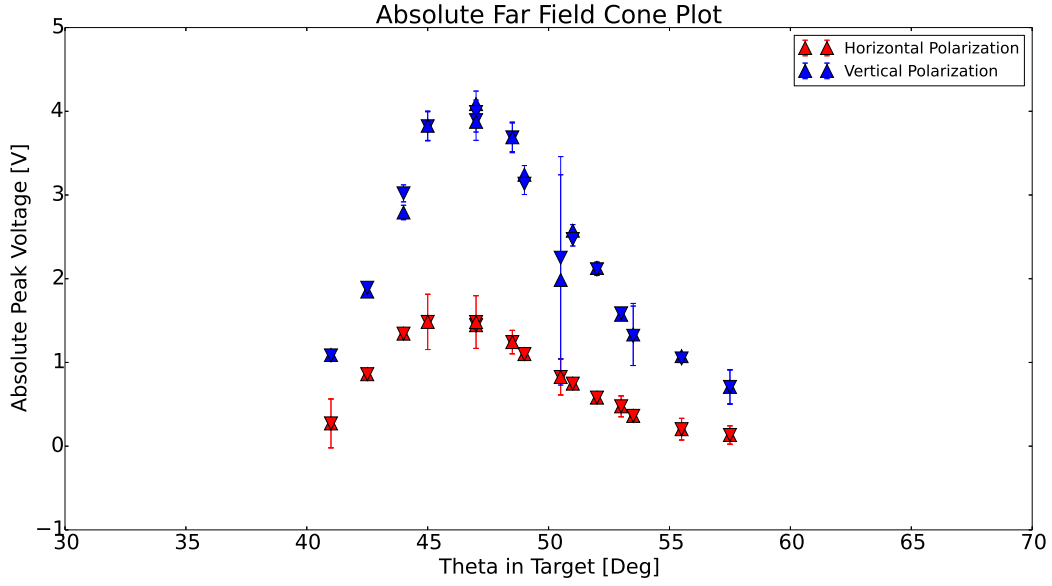
Figure 6: Far Field Cone Plot with Absolute Values of Voltage

orientations. This sign flip further confirms the assumption that the H-Pol component of the radiation results from purely the magnetic mechanism.

When the absolute value of the voltages is plotted (Figure 6), the two H-Pol curves appear to align, supporting the idea that they are in fact mirror images. In addition, the data is expected to peak in both the H-Pol and V-Pol data at approximately the same angle θ corresponding to the Cherenkov angle. A hump shape is in fact observed in both H-Pol and V-Pol data at approximately the same angle, which is interpreted as a slice of the Cherenkov cone. The peak appears to fall at approximately $47°$, relatively close with the expected value of $\theta_C = 49°$. The difference is likely due to the approximation of the particle shower as a point source located at x_{max}, estimated to be the point of beam entry into the target.

3.3   Near Field Data

Figures 7 and 8 show the same style of cone in the near field, one showing the vertical component of the peak voltage and another showing the absolute value of the horizontal component. Each plot contains points from each antenna on the array at each of the three near-field z positions and from the reference far-field z position. Points are color-coded by z position. The markers represent different magnetic field orientations: a triangle represents a point from a run with a $+y$-oriented magnetic field, an upside-down triangle represents a point from a run with a $-y$-oriented magnetic field.

The plots demonstrate clear peaks for each z position set of data. Although fewer points are present in each curve, the shape appears to be consistent with the far field case. Furthermore, the peaks appear to be centered around the same value θ. As expected, the magnitude of the peak voltage appears to decrease as the distance from the target increases, and this fall-off appears to follow a $1/R$ dependence.

Because the magnitude of the radiation is expected to decrease primarily as the inverse of R, an R correction was first applied to determine whether other near-field effects could be discerned. The individual data points were multiplied by the ratio of their radial distance (calculated from the point where the beam entered the target) to the distances of the far field positions, calculated to include refraction effects. The point of beam entry was used instead of the expected x_{max} position due to uncertainty in the exact x_{max} location. The plots, again separated into V-Pol and H-Pol, are included as Figures 9 and 10.

Upon initial inspection, the R-corrected individual cones appear to overlap relatively well; the simple R correction can account for the majority of the differences in magnitude between the different cones. The discrepancies likely originate from the
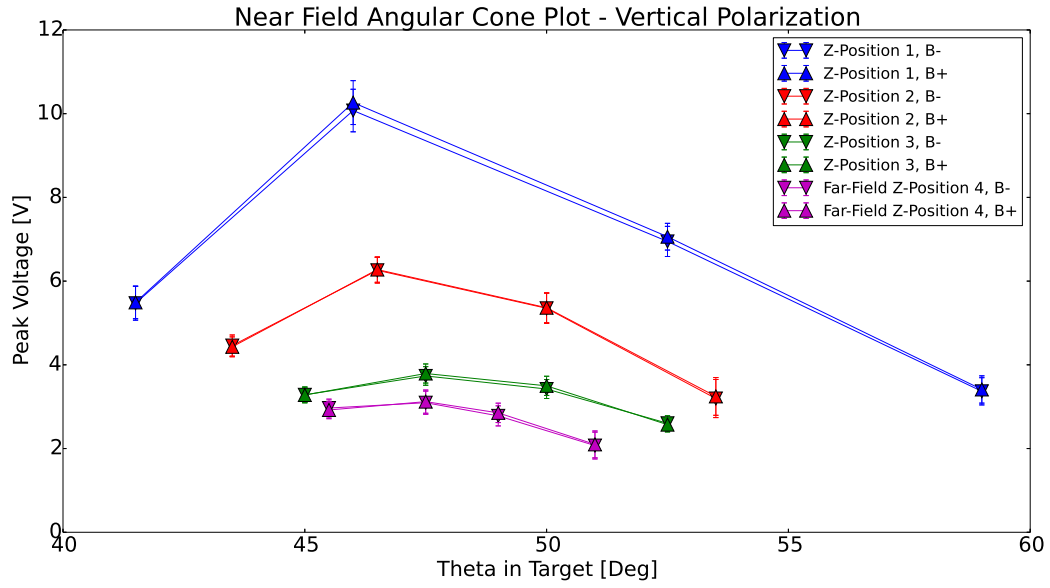
14

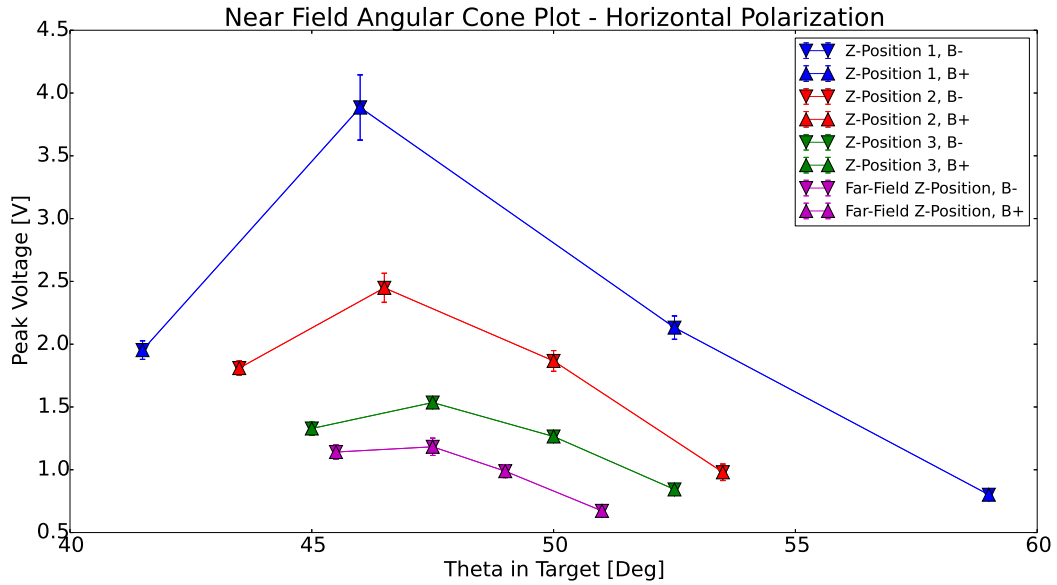Figure 7: Near Field Cone Plot (Vertically Polarized Component

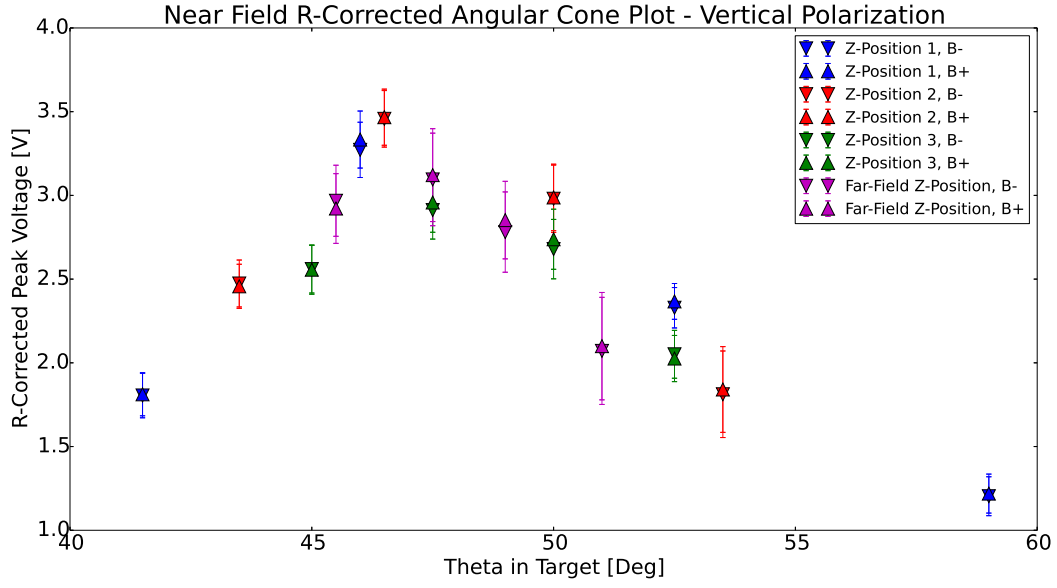Figure 8: Near Field Cone Plot (Horizontally Polarized Component

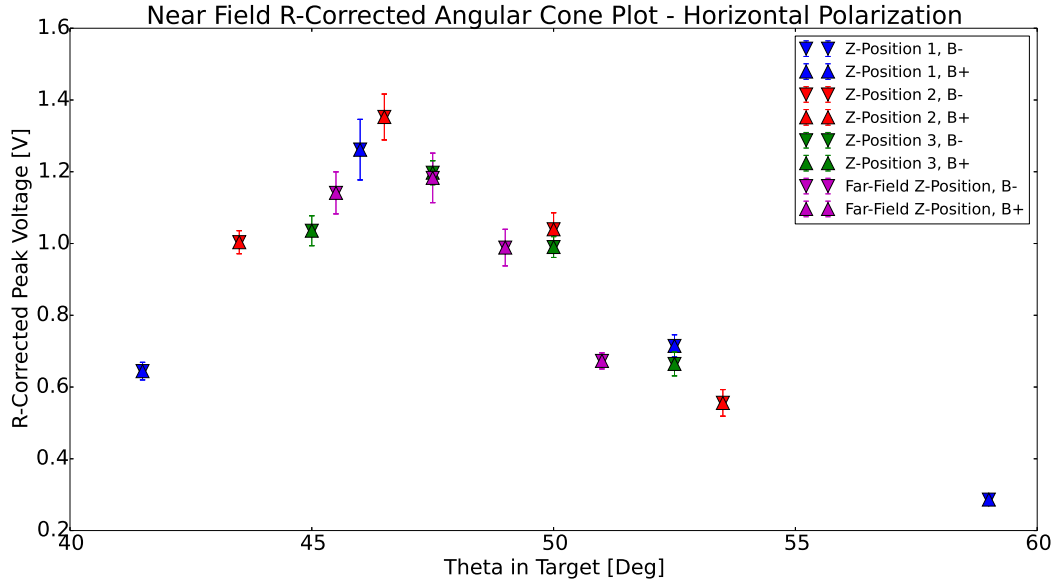Figure 9: Near Field Cone Plot (V-Pol Component) with $\frac{1}{R}$ Correction

Figure 10: Near Field Cone Plot (H-Pol Component) with $\frac{1}{R}$ Correction

16

treatment of the particle shower as an approximate point source with location at the edge of the target. Although a clear value of θ_c would require more data points, it can be estimated from the peak of the plots to be approximately 47°. This agrees well with the estimate obtained from the far-field cone plot, as well as with the expected value of 49°.

3.4 Error

Statistical error is included for both H-Pol and V-Pol data. Additional systematic error was calculated in the near-field V-Pol cone plots using the H-Pol zero-magnetic field data for each point in theta. Since theoretically the measured H-Pol peak voltage should be zero when the magnetic field is turned off, deviation can be used as a cross-polarization error estimate. Since statistical error is assumed to be uncorrelated with the cross-polarization leak error, the total V-Pol error was taken in quadrature for the statistical and cross-polarization systematic error components. Since cross-polarization error is corrected for in the H-Pol runs, such error is not included, and only statistical error is shown.

3.5 Spectral Analysis

A spectral analysis was performed to examine if and how effects of being in the near field appeared in different frequency ranges within the sensitivity of the antennas. Data from the antenna closest to the Cherenkov angle for each z-position was used for consistency across runs. Voltage pulses and Fast Fourier Transforms (FFT) were again averaged over 48 runs to minimize statistical fluctuations.

One method of spectral-analysis, the Power Spectral Density (PSD), of each event

17

was taken using the FFT as follows:

$$P(f) = \frac{2FFT(f) \times FFT^*(f)}{N \times f_{sample}}$$

where $FFT(f)$ represents the amplitude of the Fourier transform at frequency value f, N represents the total number of frequency points produced by the Fourier transform and F_{sample} represents the sampling frequency of the data aquisition system. The PSD shows the square of the complex amplitude with normalization factors of the Fourier transform for each frequency point, along with normalization factors. It offers a visualisation of the power emitted at each frequency calculated by the FFT. The PSDs of the near-field runs and reference far field run are shown in Figures 11 (V-Pol) and 12 (H-Pol).

Upon initial inspection, the PSDs appear relatively similar in shape, even in the lower frequencies where near-field interference effects would be expected. Some periodicity can be seen in both polarizations, which appears stronger in the near field than in the far field. This periodic distribution of power may suggest interference effects from delayed reflections of the radiation from within the target. As expected, the total power decreases as the antenna is moved away from the target.

Of particular interest is the magnitude of the difference between the PSD values of the near field positions and the far field reference. While a decrease in total power (manifesting as a lesser area) would be expected as the antenna moves further from the target, the decrease may mask the more subtle differences in frequency composition. A simple method of comparison is to normalize all PSD plots so that the area of each is equal to 1. These area-normalized plots are shown in Figures 13 and 14.

The normalized PSDs do show some discrepancies between the distribution of power in both the H-Pol and V-Pol cases. A residue plot demonstrating the normalized PSD
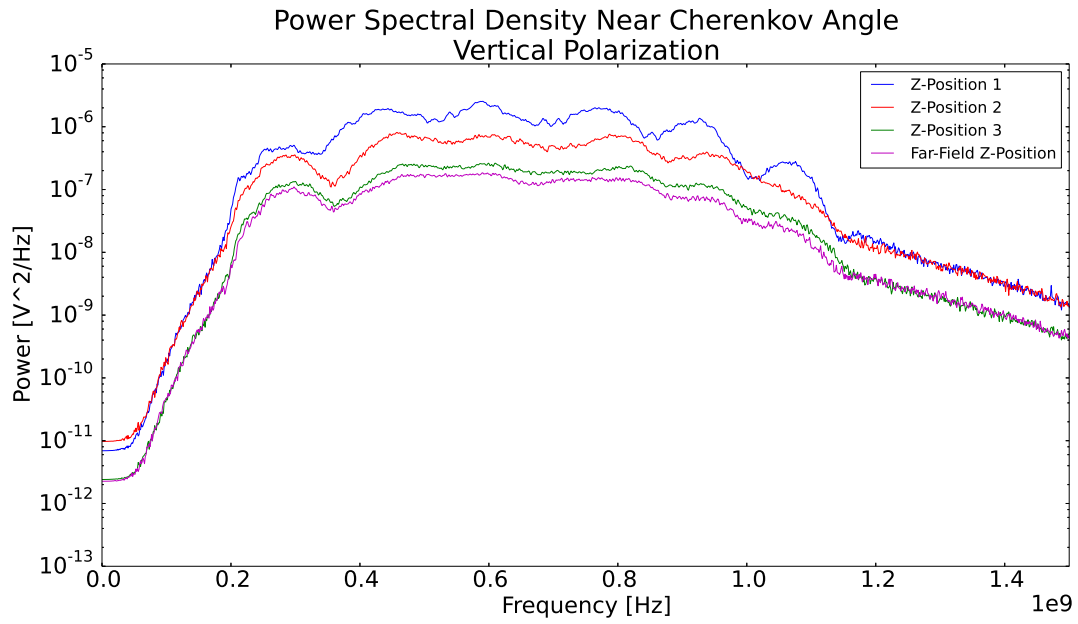
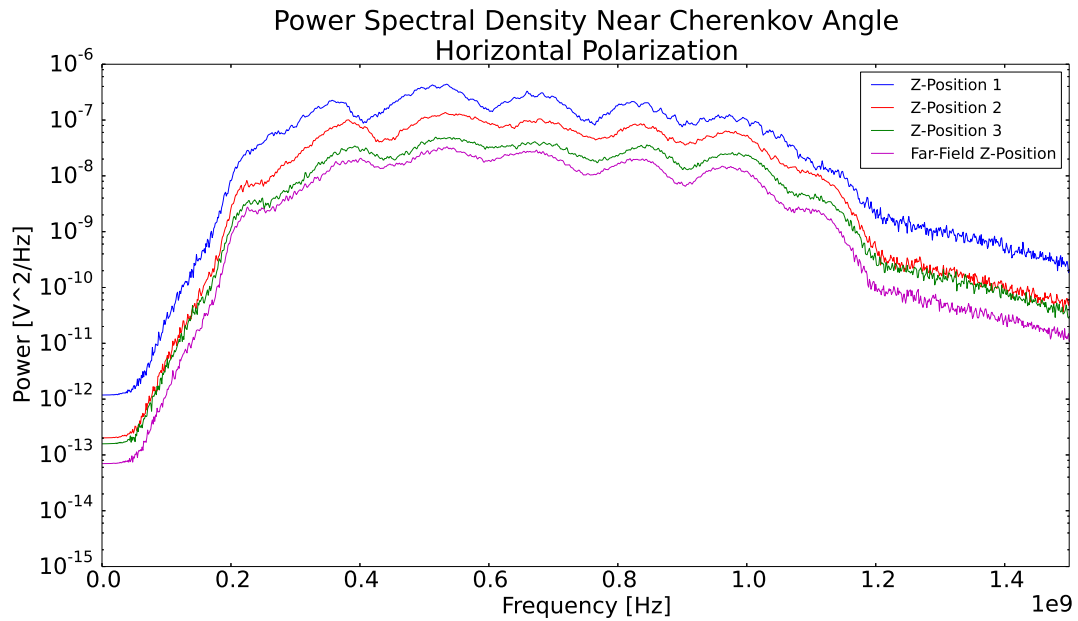Figure 11: Power Spectral Density (V-Pol Component)

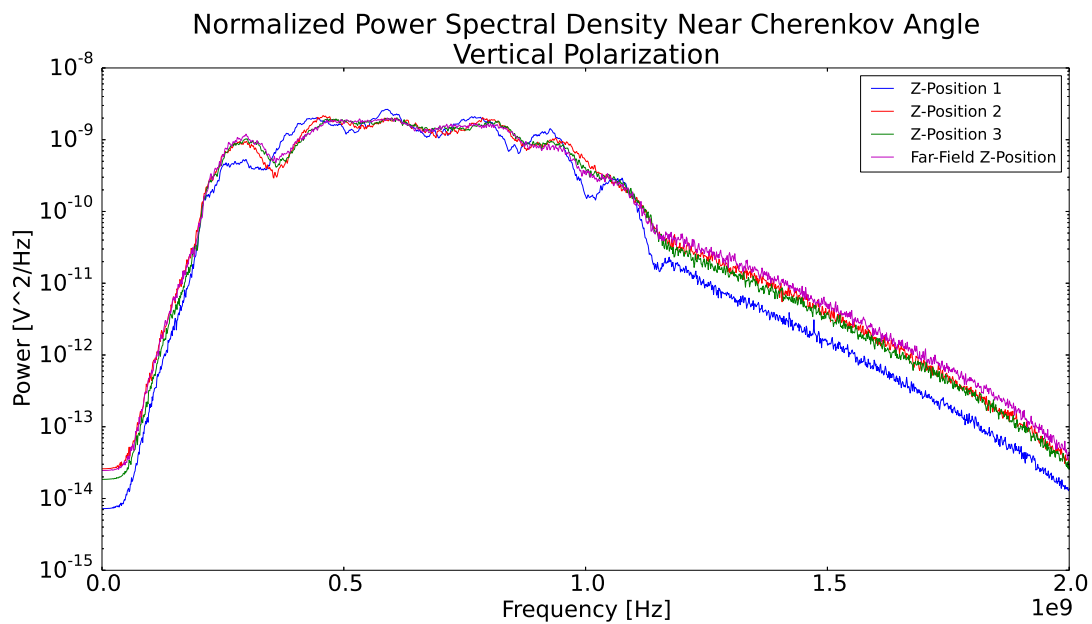Figure 12: Power Spectral Density (H-Pol Component)

19

Figure 13: Area-Normalized Power Spectral Density (V-Pol Component)
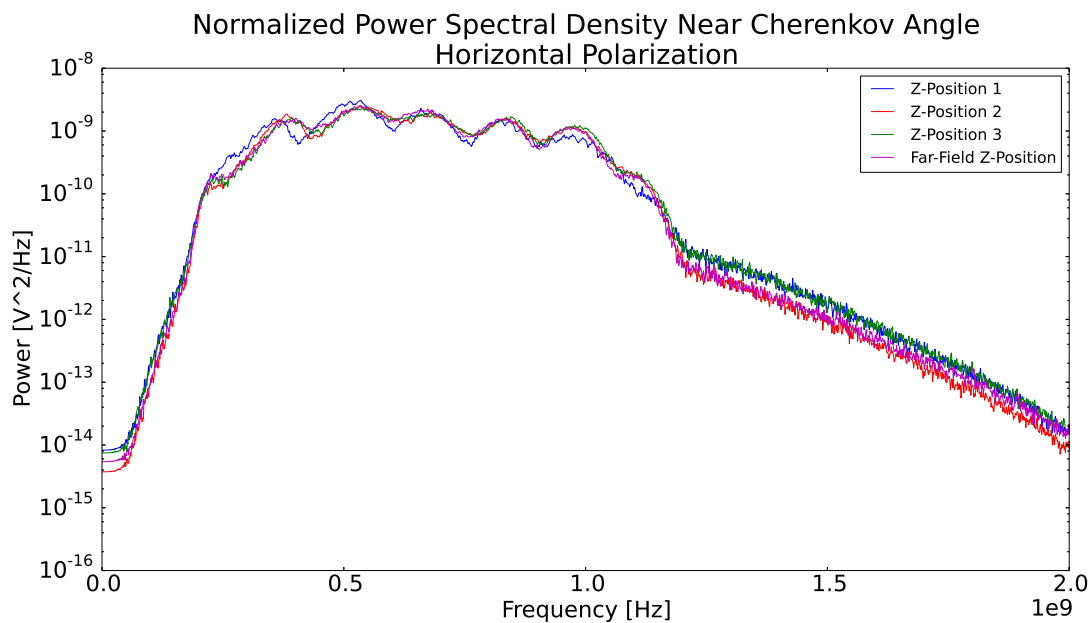

Figure 14: Area-Normalized Power Spectral Density (H-Pol Component)

20

values at each frequency minus the far field reference values provides a clearer image of such discrepancies, as shown in Figures 15 and 16. Subtracting out the far-field PSD highlights the differences in relative power over the PSD shapes themselves.

Discrepancies between the near-field and far-field PSDs appear to be focused in the lower frequencies. Since the antenna may be positioned only a few wavelengths away from the shower for these lower frequencies, the observation of near-field interference effects in this range would be expected. However, the differences are also strongly periodic, again suggesting the effects of reflections within the target by the radiation rather than true near-field interference. The lack of consistency between the variations from the far-field at the near-field z-positions further suggests that near-field interference effects are not the primary mechanism behind the observed variations.

Because reflections in the target were believed to be the source of the periodicity in the PSDs, the original voltage pulses were manipulated to try and eliminate these reflections and extract any potential near-field interference effects. A brick-wall window was applied to the pulses, which left the initial peak intact but zeroed out the pulse following its fifth zero-crossing (after this point, fluctuations are significantly lower in amplitude and are irregular in period). The windowed pulses, along with the original pulses for reference, are shown in Figures 17 and 18.

The PSDs obtained from the windowed voltage pulses are shown in Figures 19 and 20. Much of the noise is eliminated, and the periodic "bump" features disappear. The total power and overall shape of the PSDs do not appear to be substantially affected. The shapes of the PSDs are more comparable between the different z-positions with the addition of windowing, as well. Variations in the higher frequencies appear, especially in the V-Pol case, although their absolute magnitude is inflated by the logarithmic scale
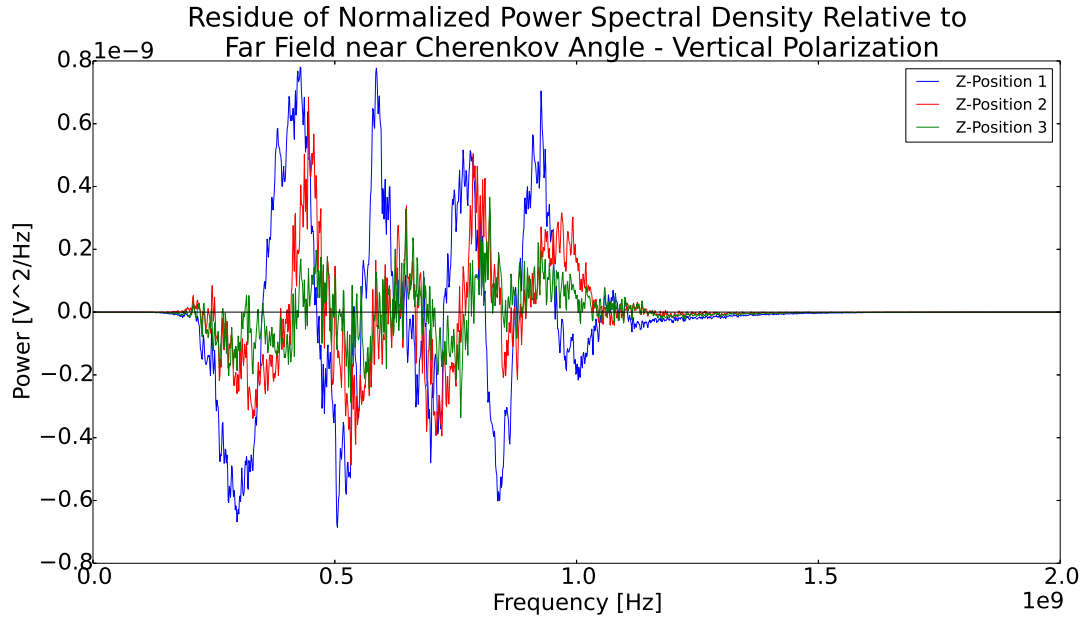
21

Figure 15: Residues of Area-Normalized Power Spectral Density (V-Pol Component)
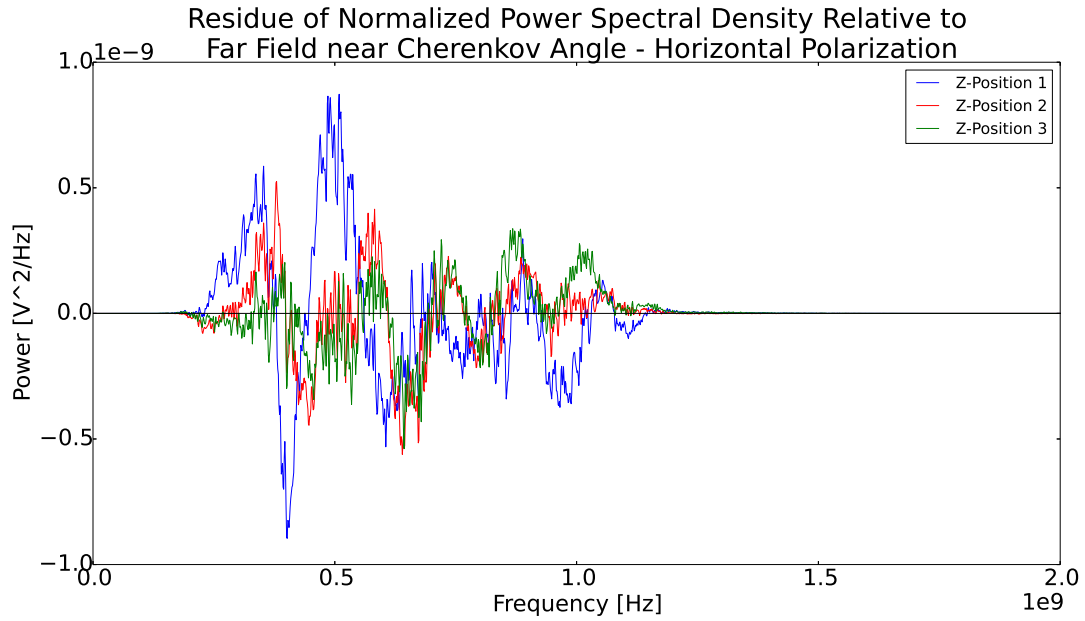

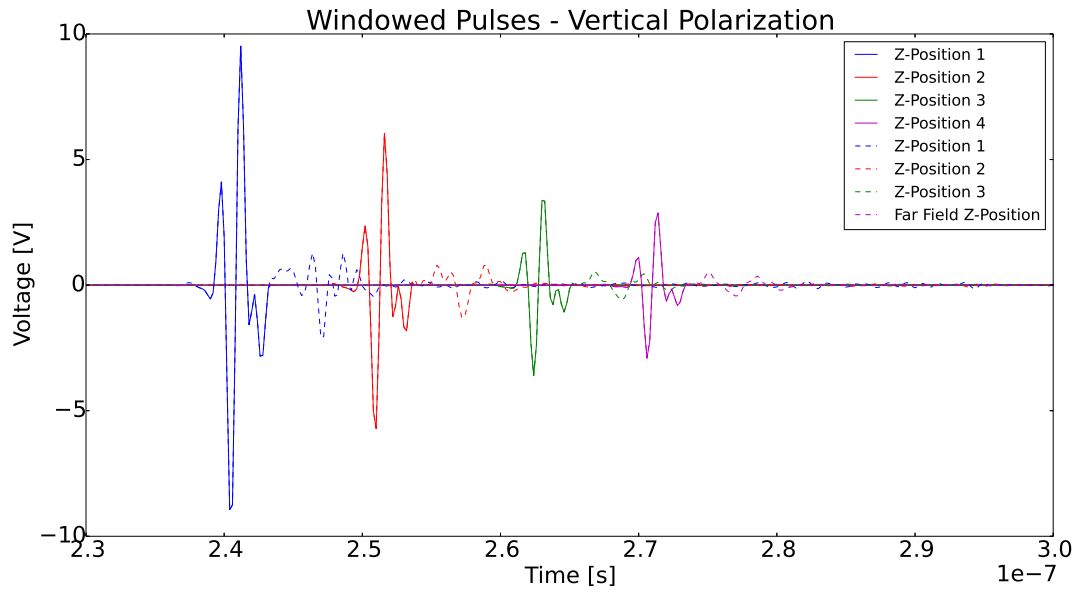Figure 16: Residues of Area-Normalized Power Spectral Density (H-Pol Component)

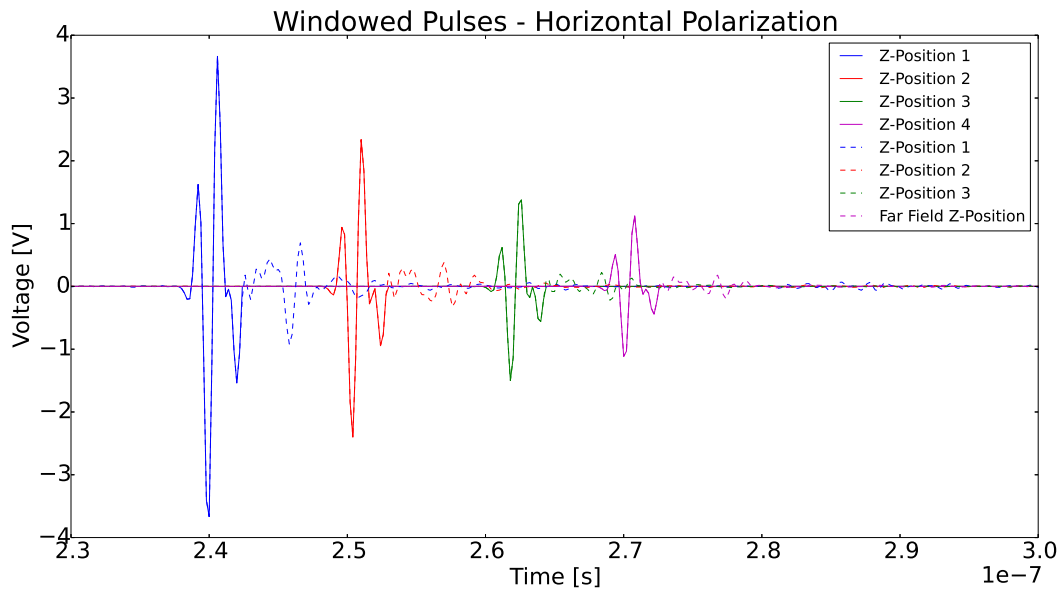Figure 17: Windowed Voltage Pulses (V-Pol Component)

Figure 18: Windowed Voltage Pulses (H-Pol Component)

of the plot. While removing the reflections successfully eliminates the periodicity of the PSD, no striking interference effects are uncovered. Again, normalizing the PSDs by area provides an easier comparison between the distribution of power among different frequency regimes, as shown in Figures 21 and 22.

No significant differences can be seen upon initial inspection between the normalized PSDs of the same polarization. Between the polarizations, the H-Pol radiation appears to be relatively stronger in the lower frequencies than in the V-Pol case. Variations manifest primarily in the higher frequencies, although their magnitude in relation to the peak power is small.

Differences in the shapes of the PSDs as the antenna moves away from the target would provide the clearest indication of near-field interference effects. As in the un-windowed case, residue plots may be used to more clearly show the discrepancies between the near-field and far-field power distribution, as shown in Figures 23 and 24.

The windowed-PSD residue plots show some discrepancies between the distribution of power in the near and far field within the lower frequencies (corresponding to wavelengths above ≈ 0.2 m) for both polarizations. However, the effects appear to be inconsistent as the antenna is moved away from the target. Furthermore, the differences still appear to be somewhat periodic in nature, suggesting the effects of reflections are still present. Frequencies above approximately 120 MHz appear to be unaffected. Since these frequencies correspond with $\lambda \approx 0.25$m, these components are reasonably outside of the near-field range, even in the near-field runs, and so their agreement is expected. Because of the likely presence of in-target reflections, the low-frequency differences in power cannot be clearly attributed to near-field effects. Further study is needed in order to determine the root cause of the observed spectral behavior.
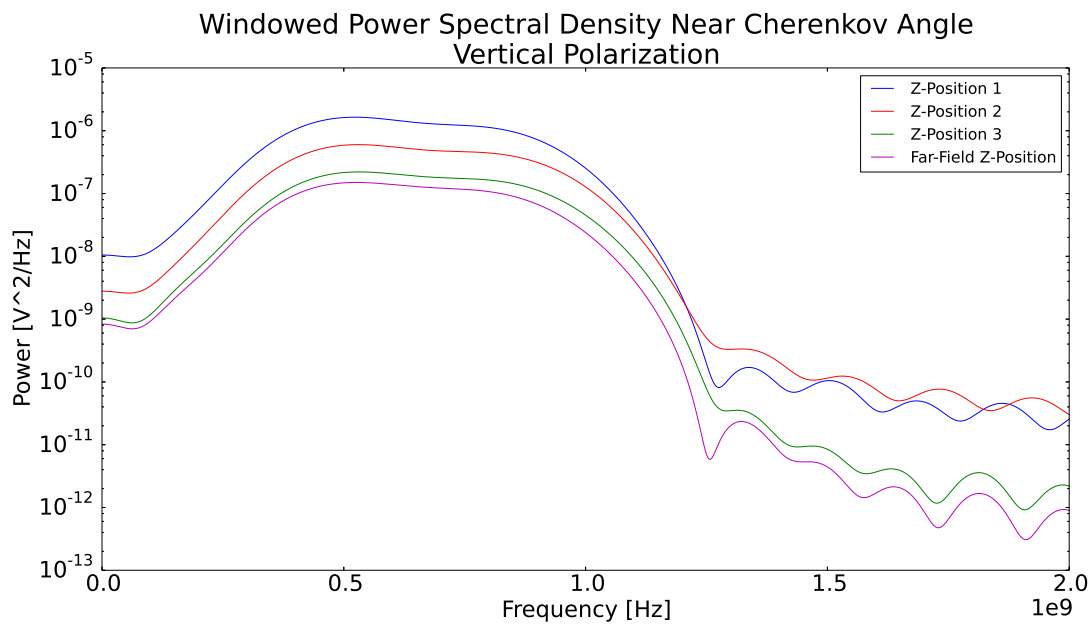
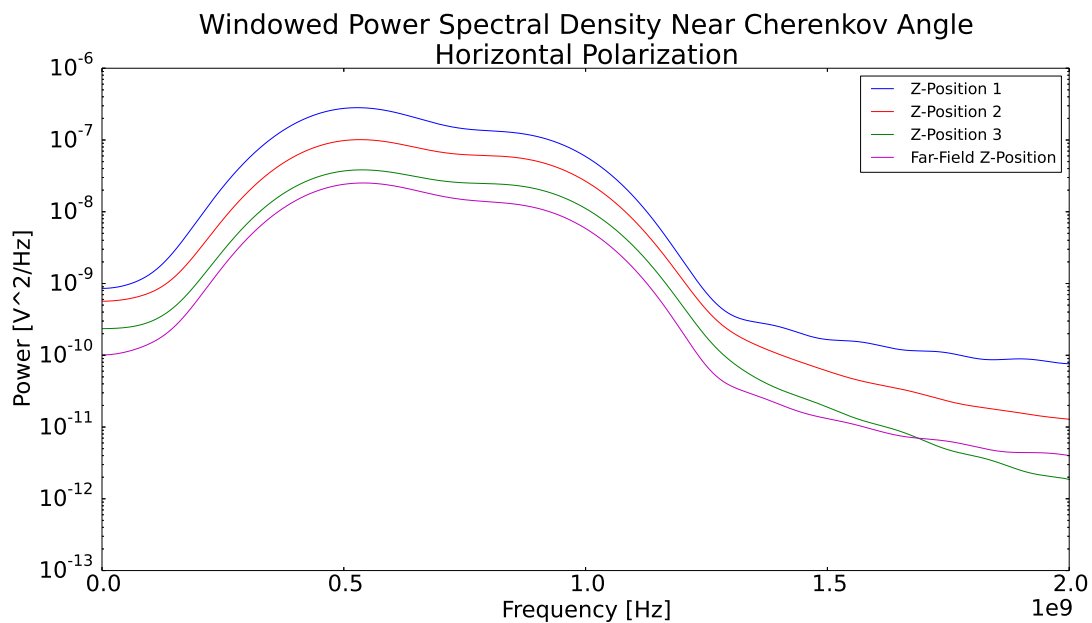Figure 19: PSDs from Windowed Voltage Pulses (V-Pol Component)

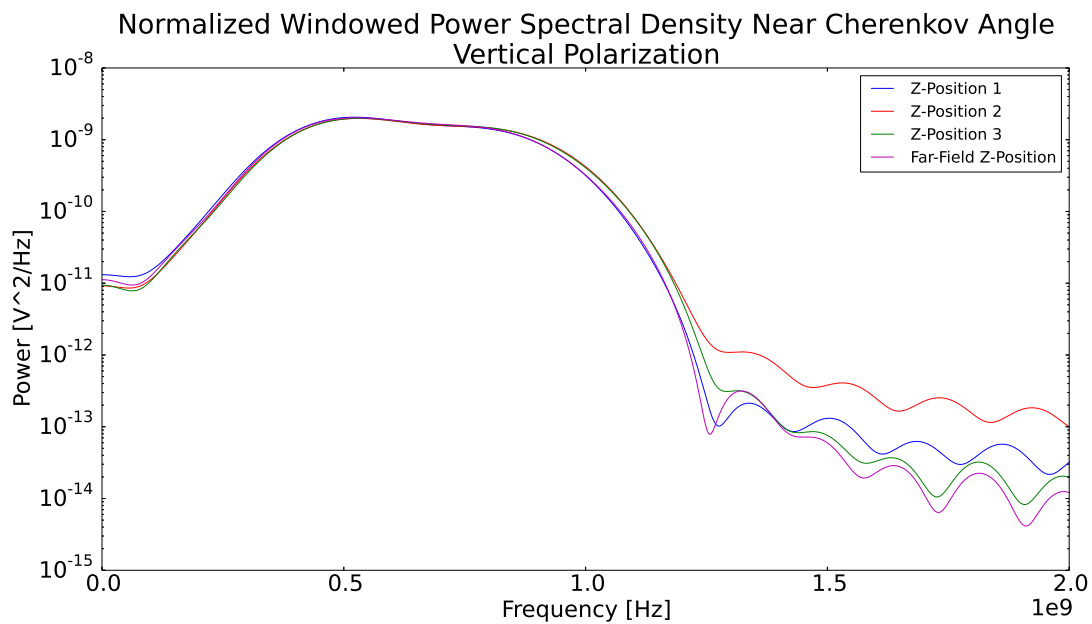Figure 20: PSDs from Windowed Voltage Pulses (H-Pol Component)

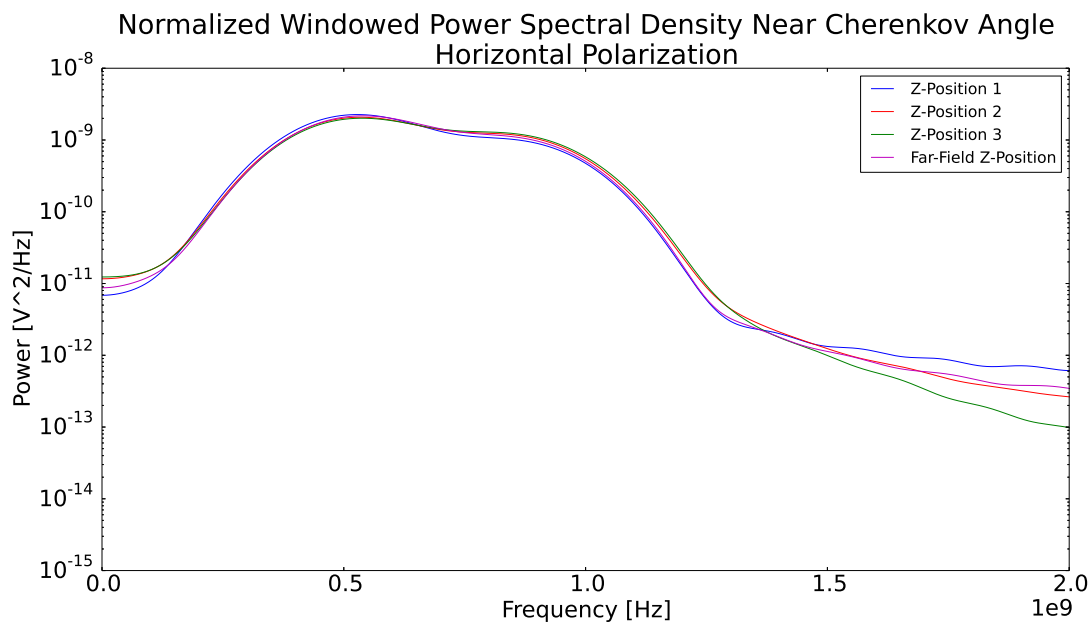Figure 21: Area-Normalized, Windowed PSDs (V-Pol Component)

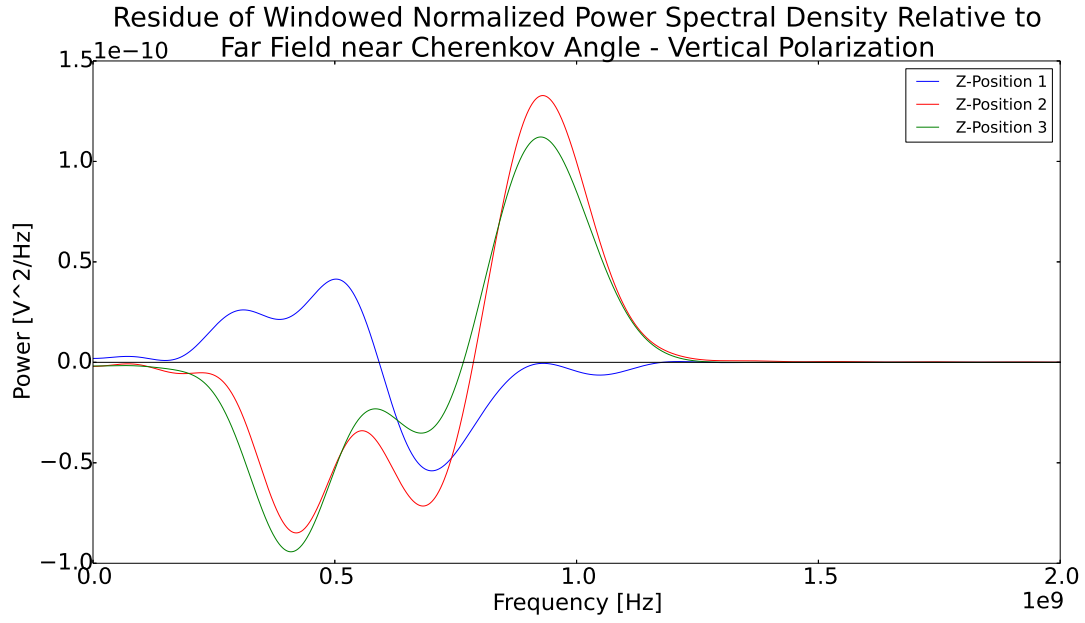Figure 22: Area-Normalized, Windowed PSDs (H-Pol Component)

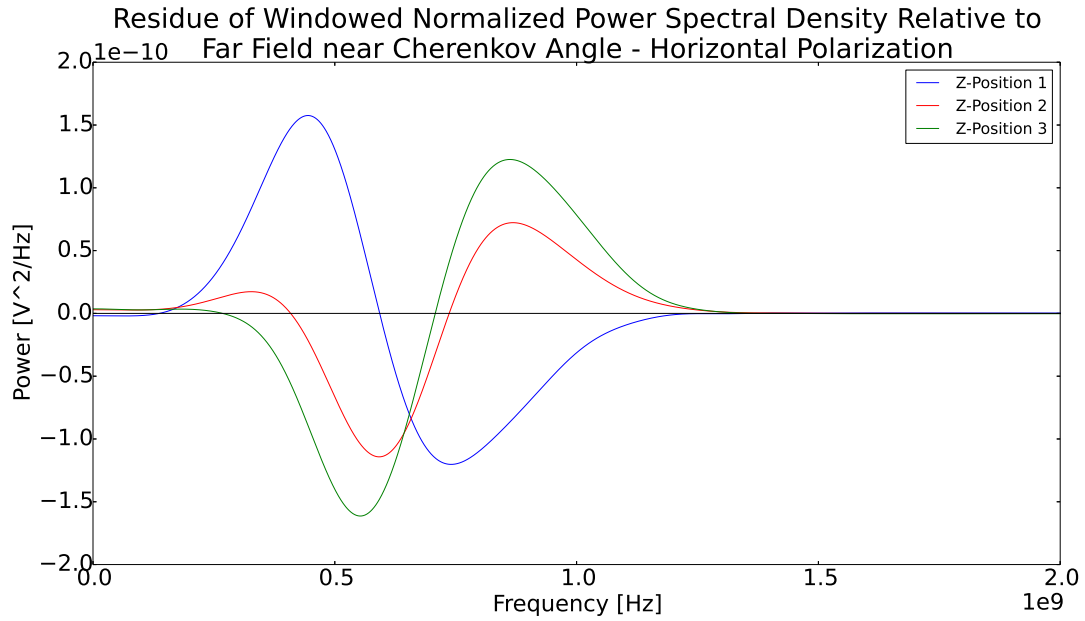Figure 23: Residue of Area-Normalized, Windowed PSDs (V-Pol Component)

Figure 24: Residue of Area-Normalized, Windowed PSDs (H-Pol Component)

4   Conclusions

Distinct cone-shapes can be observed from the peak voltage data from each z position. The magnitude of the cone-shapes appears to be relatively similar regardless of the direction of the magnetic field, and, in the case of the vertical component, regardless of the presence or direction of a magnetic field. The magnitude of the peak voltage decreases as the antenna array is moved to a more distant z position. The peak of each cone shape appears to correspond with the same angle θ, or the predicted Cherenkov angle, with a significant decrease in voltage observed far from $\theta = \theta_c$ in both the near field and far field data. Furthermore, a $\frac{1}{R}$ correction appears to correct the near-field cones well, indicating that the $\frac{1}{R}$ effects may be dominating, even in the near field. A spectral analysis of the voltage pulses indicates a decrease in total power as the antenna is moved away from the target. Discrepancies in the distribution of power among different frequency ranges can also be seen as the antenna moves away from the target. However, the origin of these effects remain unclear, and they are likely the result of reflections within the target rather than near-field interference.

5   Acknowledgements

References

[1] G. A. Askaryan. Coherent Radio Emission from Cosmic Showers in Air and in Dense Media. *Soviet Journal of Experimental and Theoretical Physics*, 21:658, September 1965.

[2] K. Belov. Geosynchrotron radio emission from extensive air showers. a proposal for an experiment in end station a at slac national accelerator laboratory., October 2012.

[3] P. W. Ghoram et al. Observations of the askaryan effect in ice. *SLAC PUB*, 2007.

[4] S. Hoover et al. Observation of ultrahigh-energy cosmic rays with the anita balloon-borne radio interferometer. *Physical Review Letters*, October 2010.

[5] John David Jackson. *Classical Electrodynamics*. John Wiley & Sons, Inc., 1962.

[6] John Kraus. *Antennas*, chapter 2. McGraw Hill Book Company, 2 edition, 1988.

[7] J. Matthews. A Heitler model of extensive air showers. *Astroparticle Physics*, 22:387–397, January 2005.